28th Symposium on Naval Hydrodynamics
Pasadena, California, September 12 ~17, 2010

Numerical simulations of wave breakings around a wedge-shaped bow

Zhaoyuan Wang, Jianming Yang, Frederick Stern
(IIHR-Hydroscience & Engineering, University of Iowa,
Iowa City, IA 52242, USA)

ABSTRACT

Flows around a wedge-shaped bow are simulated with the aim of investigating the wave breaking mechanism and small scale features of ship bow waves. The wedge geometry used in the experimental study of Waniewski et al. (2002) is chosen with the flow conditions at Re = 1.64×10^5 and Fr = 2.93. The bow wave structure, wave breaking process and air entrainment are studied. The predicted overall bow wave profile, surface disturbances on the wave crest, and plunging jet shape are similar to the experimental observations. The computed wave contact line elevation is very close to the flume model case of the experiment, but is below the towing tank case. The possible reasons of the under-prediction of the wave elevation are discussed.

INTRODUCTION

Breaking waves, spray formation, and air entrainment around ships are the main sources of the underwater sounds and white-water wakes, which are of great importance for signature of ships. These flow phenomena occur on a large range of temporal and spatial scales. At small scales, spray formation and air entrainment in the contact line region depend on the length scales which are orders of magnitude smaller than the length of the ship with correspondingly small time scale. For the large scales, the overall structures include wave breakings along the hull and the induced vortices, instabilities, separations and scars, etc. Understanding the small scale physics and capturing their effects on the large scale features are of primary importance for ship hydrodynamics.

Experimental and computational studies have been conducted for the flows of a surface-piercing flat plate with focus on the wave induced effects on the flat plate boundary layer below the juncture region (Stern, 1986; Stern et al., 1989; Stern et al., 1993). More recent experimental and computational studies focused on the juncture region and turbulence modeling using towed, two-dimensional laser-doppler velocimetry (LDV) and RANS and large-eddy simulation (LES) methods for flat free surface (Longo et al., 1998; Sreedhar and Stern, 1998a, b). The juncture region experiment (Longo et al.,1998) is extended to include wave effects using servomechanism wave gauges (Kang et al., 2008). It is observed that the interface appears always broken in the contact line region even for the case with a smooth wave field. Air is entrained into the boundary layer at the contact line region due to the interaction of the contact line with the solid surface. A string of bubbles can be generated near the solid wall usually with small bubble sizes. For flows past a blunt leading edge, such as NACA0024 foil, the bow wave breaks and wraps around the bow with similar features to spilling breakers (Metcalf et al., 2006) at a *Fr* number of 0.37. Wave induced flow separation occurs and reattaches to the foil surface resulting in a wall-bounded separation bubble. The complexity of unsteady, wave-induced, boundary layer separation makes the experimental measurements difficult. With the combined CFD studies (Kandasamy et al., 2009 and Xing et al., 2007), more detailed flow description is provided. Three main instabilities, namely the initial shear-layer instability, Karman-like shedding and flapping of the separation bubble, were found in the unsteady Reynolds-averaged Navier-Stokes (URANS) study (Kandasamy et al., 2009). These instabilities are difficult to be identified in both the DES study (Xing et al., 2007) and experimental study (Metcalf et al., 2006) due to the numerous small-scale vortices in the separation region. There are limitations in both of the two CFD studies. The complicated flow structures at the interface as shown in the experimental images, such as splashing, breaking waves, air entrainment and free surface induced turbulence observed in the experiments, cannot be resolved since a single phase flow solver (air effect is neglected) and relatively less accurate interface modeling methods were used. These unresolved flow structures at the interface might affect the global flow patterns and turbulence.

Previous studies are mainly focused on the global structure of ship flows, such as the wave

elevation, scars, and vortices. The small scale details of interface breaking, spray formation, and air entrainment are not well understood. Ship bow waves exhibit both large and small scale features. The most prominent large scale feature is the Kelvin bow wave pattern scaled by *Fr*; however, for sufficiently large *Fr* and depending on bow shape, spilling and/or plunging breaking occurs and induces vortices and scars additionally scaled by *Re* and *We*. Small *Re* and *We* inhibit breaking, i.e., in general model scale flows exhibit reduced breaking compared to full scale, and smaller models display reduced breaking compared to larger models. A recent complementary EFD and CFD study has documented bow wave breaking and induced vortices and scars for model 5415 for $Fr = 0.35$ using CFDShip-Iowa Version 4 (Olivieri et al., 2007; Wilson et al., 2007). The most prominent small scale feature is the bow wave crest formation of thin overturning sheets which break up into spray. *Re* and *We* scale effects are large such that replication of full scale phenomena of the small scale features of ship bow waves is difficult even with large models. The extent of the thin sheets is drastically reduced and remains attached, as shown by Stern et al. (1996) for the Series 60.

However, studies for wedge flows by Waniewski et al. (2002) and Karion et al. (2004) display and document the structure of bow waves (thin water sheet formation, overturning sheet with surface disturbance, fingering and breaking up into spray, plunging and splashing, and air entrainment) with valuable experimental data provided such as wave elevation, extent of wave breaking, spray droplets size and number. These two studies are summarized in Table 1. In Waniewski et al. (2002) the bow waves are created by a deflecting plate mounted at an angle in a flume, the towing tank experiments are also conducted with two wedge models. Typical bow wave profile obtained in the towing tank experiment shows a thin liquid sheet is created at the leading edge of the wedge, and it continues to ride up on the side wall. This thin liquid sheet starts to separate from the side wall as it reaches its maximum height. Once the crest reaches its maximum height, an overturning jet is formed and plunges back onto the undisturbed free surface. A large area of splash is generated at the wake of the wedge due to wave plunge and air entrainment. Noblesse et al. (2008) proposed a series of simple analytical relations for a wedge-shaped bow wave based on the experimental measurements and elementary fundamental considerations, which define the main characteristics of a ship bow (wave height, wave crest location and profile, and flow steadiness or unsteadiness) in terms of ship speed *U*, draught *D* and waterline entrance angle 2θ. A computational study has been carried out by Broglia et al. (2004) with the results compared with the experimental data (Waniewski et al., 2002). Since a single phase level set method was used for the free surface tracking, the small scale interface structures were not captured. The mechanism of the liquid sheet disturbance, figuring, pinching off drops and spray formation has not been thoroughly studied.

Herein, flows around a wedge-shaped bow are numerically simulated with the aim of investigating the wave breaking mechanism and small scale features of ship bow waves. The study (Waniewski et al., 2002) was selected as test cases to validate the capability of the code of CFDShip-Iowa Version 6 (Yang and Stern, 2009; Wang et al., 2009) for small scale features of ship bow waves. Comparison with the experimental results obtained by Karion et al. (2004) will be included in the future work. The simulations are carried out using a Cartesian grid solver first with the sharp interface, coupled level set and volume-of-fluid (CLSVOF) and immersed boundaries methods; and an orthogonal curvilinear grid solver (Suh et al., 2010) is also used in order to increase the grid resolutions near the wall.

COMPUTATIONAL METHODS

CFDShip-Iowa version 6, a Cartesian and orthogonal curvilinear grid solver for two-phase incompressible flows recently developed at IIHR (Yang and Stern, 2009; Wang et al, 2009; Suh et al., 2010), is used for the computations. In this solver, the interface is represented by a CLSVOF method. A ghost fluid methodology is adopted to handle the jump conditions across the interface. A sharp embedded boundary method is used to handle the complex immersed boundaries on Cartesian grids.

For simplicity, vector notation will be used for all equations without regard to the coordinate systems in the following parts unless otherwise declared. The governing equations in indicial notation for orthogonal curvilinear coordinates are given in the Appendix.

Mathematical Modelling

Navier-Stokes Equations and Jump Conditions

For the incompressible viscous flows of two immiscible fluids with constant properties, the Navier-Stokes equations are given as follows

$$\frac{\partial \mathbf{u}}{\partial t} + \mathbf{u}\cdot\nabla\mathbf{u} = \frac{1}{\rho}\nabla\cdot\left(-p\mathbf{I}+\mathbf{T}\right)+\mathbf{g}\,, \tag{1}$$

$$\nabla\cdot\mathbf{u} = 0\,, \tag{2}$$

where t is time, $\mathbf{u}$ is the velocity vector, p is pressure, $\mathbf{I}$ is the unit diagonal tensor, ρ is density, $\mathbf{g}$ represents the acceleration due to gravity, and $\mathbf{T}$ is the viscous stress tensor defined as

$$\mathbf{T} = 2\mu\mathbf{S}, \tag{3}$$

with μ the dynamic viscosity and $\mathbf{S}$ the strain rate

$$\mathbf{S} = \frac{1}{2}\left[\nabla\mathbf{u} + (\nabla\mathbf{u})^T\right], \tag{4}$$

where the superscript T represents transpose operation. Density and viscosity are discontinuous across the interface, which is a function of time and space. They will be defined using LS function later.

Since the fluids considered here are viscous and no phase change occurs, the velocity across the interface Γ is continuous:

$$[\mathbf{u}] = 0, \tag{5}$$

where [ ] denotes the jump at the interface, i.e., $f_L^I - f_G^I$ for a variable f with superscript I representing interface. The exact jump condition for stress is

$$\left[\mathbf{n}\cdot\left(-p\mathbf{I} + \mu\left(\nabla\mathbf{u} + (\nabla\mathbf{u})^T\right)\right)\cdot\mathbf{n}\right] = \sigma\kappa, \tag{6}$$

where $\mathbf{n}$ is the unit vector normal to the interface, σ is the coefficient of surface tension, and κ is the local curvature of the interface. With a smoothed viscosity and continuous velocity field, the stress jump condition reduces to

$$[p] = p_L^I - p_G^I = -\sigma\kappa. \tag{7}$$

Interface Modeling

The interface is represented by the LS function which is corrected to enforce mass conservation with the aid of the VOF function. The LS function, ϕ, is defined as a distance function which is negative in the air, positive in the liquid, and zero at the interface. The VOF function, F, is defined as the liquid volume fraction in a cell with its value in between zero and one in a surface cell and zero and one in air and liquid, respectively.

The LS function and the VOF function are advanced using the following equations, respectively,

$$\frac{D\phi}{Dt} = \frac{\partial\phi}{\partial t} + (\mathbf{u}\cdot\nabla)\phi = 0, \tag{8}$$

$$\frac{DF}{Dt} = \frac{\partial F}{\partial t} + (\mathbf{u}\cdot\nabla)F = 0. \tag{9}$$

To keep the LS function as a signed distance function in the course of evolution, the LS function is re-initialized by iterating the following equation (Sussman et al., 1994),

$$\frac{\partial\phi}{\partial\tau} + S(\phi_o)\left(|\nabla\phi| - 1\right) = 0, \tag{10}$$

where τ is the pseudo time and $S(\phi_o)$ is the numerically smeared-out sign function

$$S(\phi_o) = \frac{\phi_o}{\sqrt{\phi_o^2 + h^2}}, \tag{11}$$

with ϕ_o the initial values of ϕ and h a small distance, usually the grid cell size, to smear out the sign function.

Each phase of constant density and viscosity can be defined using the LS function in the computational domain and sharp jumps of the fluid properties occur at the phase interface. In this study, the density keeps its sharp jump and the viscosity is smoothed over a transition band across the interface,

$$\begin{aligned}\rho &= \rho_G + (\rho_L - \rho_G)H(\phi)\\ \mu &= \mu_G + (\mu_L - \mu_G)H_\varepsilon(\phi)\end{aligned}, \tag{12}$$

where the subscripts G and L represent gas and liquid phase, respectively, the stepwise Heaviside function is

$$H(\phi) = \begin{cases}1 & \text{if} \quad \phi \ge 0\\ 0 & \text{if} \quad \phi < 0\end{cases}, \tag{13}$$

and the smoothed Heaviside function is

$$H_\varepsilon(\phi) = \begin{cases}1 & \text{if} \quad \phi > \varepsilon\\ \frac{1}{2}\left[1 + \frac{\phi}{\varepsilon} + \frac{1}{\pi}\sin\left(\frac{\pi\phi}{\varepsilon}\right)\right] & \text{if} \quad |\phi| \le \varepsilon\\ 0 & \text{if} \quad \phi < -\varepsilon\end{cases}, \tag{14}$$

where $\varepsilon = 1.5\Delta x$.

The geometric properties, i.e., the normal vector and curvature, can be estimated readily from the LS function,

$$\mathbf{n} = \frac{\nabla\phi}{|\nabla\phi|}, \tag{15}$$

$$\kappa = \nabla\cdot\left(\frac{\nabla\phi}{|\nabla\phi|}\right). \tag{16}$$

Numerical Method

Navier-Stokes Solver

The finite differences method is used to discretize the Navier-Stokes equations on a non-uniform staggered Cartesian grid, in which the velocity components u, v, and w are defined at centers of cell faces in the x, y, and z directions, respectively, and all other variables, i.e., p, ϕ, ρ, μ, and ν_t are defined at cell centers. A semi-implicit time-advancement scheme is adopted to integrate the momentum equations with the second-order Crank-Nicolson scheme for the diagonal viscous terms and the second-order Adams-Bashforth scheme for the convective terms and other viscous terms. A four-step fractional-step method (Choi and Moin, 1994) is employed for velocity-pressure coupling, in which a pressure Poisson equation is solved to enforce the continuity equation. The convective terms are discretized using a third-order QUICK scheme (Leonard, 1979) and higher-order WENO schemes (Jiang and Shu, 1996) are available. All other terms are discretized with the standard second-order central difference scheme. The resulting tridiagonal linear equations are solved with the parallel

tridiagonal system solver (Mattor et al., 1995). The parallelization is done via a domain decomposition technique using the MPI library. The pressure Poisson equation is solved using a multigrid-preconditioned Krylov subspace solver from the PETSc library (Balay et al., 2002). A new semi-coarsening multigrid Poisson solver from the HYPRE library from Lawrence Livermore National Laboratory (Falgout et al., 2006) has been added recently. In general, the Poisson solver is the most expensive part of the whole algorithm.

Interface Tracking/Capturing

The level set advection and reinitialization equations are solved using a third-order TVD Runge-Kutta scheme (Shu and Osher, 1988) for time advancement and the fifth-order HJ-WENO scheme (Jiang and Peng, 2000) for spatial discretization. The solution time of these equations does not pose a significant overhead as they are solved in a narrow band several grid-cells wide as detailed in Peng et al. (1999).

The CLSVOF method has been developed in order to improve the mass conservation property of the level set method. The interface is reconstructed via a PLIC scheme and the level set function is re-distanced based on the reconstructed interface. The interface is advected using a Lagrangian method with a second-order Runge-Kutta scheme for time integration. An efficient level set re-distance algorithm is explored, which significantly simplifies the complicated geometric procedure by finding the closest point on the reconstructed interface directly without considering the interface configuration in each computational cell. It is especially efficient for three-dimensional cases where various possibilities of the interface configuration exist. The performance of the CLSVOF method has been evaluated through the numerical benchmark tests and validation and application examples, where mass conservation has been well preserved. The details of this CLSVOF method for the Cartesian grid are given in Wang et al. (2009). The extension to the general and orthogonal curvilinear grids has been recently accomplished at IIHR. The implementation algorithm of the CLSVOF method for the curvilinear grid will be presented in a separate paper.

Immersed Boundary Treatment

A sharp interface immersed boundary method (Yang et al., 2008) is adopted here to treat the immersed boundaries/bodies in a non-uniform Cartesian grid. In this approach, the grid generation for complex geometries is trivial since the requirement that the grid points coincide with the boundary, which is imperative for body-fitted methods, is relaxed; while the solution near the immersed boundary is reconstructed using momentum forcing in a sharp-interface manner.

To summarize, the first step is to establish the grid-interface relation with a given immersed boundary description, such as parametrized curve/surface or a triangulation. In this step all Cartesian grid nodes are split into three categories: (1): fluid-points, which are points in the fluid phase; (2) forcing points, which are grid points in the fluid phase with one or more neighboring points in the solid phase; (3) solid-points, which are points in the solid phase. The Navier-Stokes solver described in the previous section is applied on all points of the Eulerian grid as if the fluid/solid interface was not present. The effect of the immersed boundary on the flow is introduced through the discrete forcing function, which is computed only at the forcing points by directly enforcing the boundary conditions. In general, the velocity at the forcing points can be computed by means of linear interpolation that involves the projection of the forcing point on the interface and two points in the fluid phase.

High Performance Computing

It is well-known that the simple topologic structure of Cartesian grids is extremely favorable for coarse-grain parallelization. A simple domain decomposition technique is used in CFDShip-Iowa V6 where the Cartesian grid is divided into uniform pieces, each of which resides in one processor. In Yang et al. (2007), only slab decomposition was used and the maximum number of processors that could be used was determined by the number of grid points in one direction. In this study, domain decomposition in all three directions has been implemented, which facilitates the use of hundreds of processors even with coarse grids. All inter-processor communications for ghost cell information exchange have been changed into non-blocking mode. In general, optimal load balance can be achieved except for a small amount of overhead due to interface and immersed boundary treatment, which may be unevenly distributed over processors. Parallel I/O using MPI2 have been implemented such that all processors read from and write to one single file simultaneously, which is much more effective than one or a few processors receive data from all processors and write to one or a few files and more convenient than every processor writes its own data files.

SIMULATION RESULTS

Computational Setup

The geometry of the wedge, the computational domain and boundary conditions are shown in Figure 1. The geometry of the wedge is similar to the large wedge model used by Waniewski et al. (2002). The side length of the wedge is L = 0.75 m, and the height of the wedge is H = 1.0 m. The half wedge angle is θ = 26° and the flare angle φ = 0°. On the orthogonal curvilinear grid, the wedge geometry is the same as that on the Cartesian grid, except that the sharp edge corners are rounded with an arc of a small radius (Fig. 1c).

In the case considered here, the water depth is d = 0.0745 m and the upstream velocity is U = 2.5 m/s, the corresponding Reynolds number, $\mathrm{Re} = \rho U d/\mu$, is 1.64×10^5, and the Froude number, $\mathrm{Fr} = U/\sqrt{gd}$, is 2.93. The simulations are conducted on a computational domain of x = [-1.0 m, 6.0 m], y = [-0.5 m, 0.5 m] and z = [0.0 m, 3.0 m] for the Cartesian grid. For the orthogonal curvilinear grid, x = [-5.33 m, 4.55 m], y = [-0.0745 m, 0.6 m], and z = [0 m, 5 m]. Uniform inflow and convective outflow boundary conditions are used. Slip wall boundary conditions are imposed at all the other boundaries. A uniform velocity field same as the upstream velocity is prescribed to the entire computational domain at the t = 0. Two non-uniform grids are used for both the Cartesian and orthogonal curvilinear grids. The four simulation cases are summarized in Table 2. The grid structures for the Cartesian and orthogonal curvilinear grids are shown in Fig. 2, where both grids are refined near the solid surface.

Bow Wave Profile and Surface Disturbance

Figure 3 shows the computed bow wave profile compared with the experimental video image. As shown in the figure, the overall structure of the wave is very similar to the experimental observation, such as the thin liquid sheet at the leading edge of the bow, overturning jet, jet plunging onto the free surface, and splashes at the wake. As the liquid sheet overturns, the sheet is stretched and fingered up, and some "cylindrical drops" then pinch off from the liquid sheet, when the detached drops impact the water surface, a spray region is created.

Surface disturbances were observed on the crest of the wave in the experiments (Waniewski et al., 2002). These surface disturbances appeared to be “finger-like” structures. Similar surface disturbances are also found in the current simulations as shown in Figure 4. At the leading portion of the wedge, the liquid sheet is relatively smooth. Surface disturbance starts at the middle portion and develops at the trailing portion. However, small disturbances can also be found at the leading edge for the case on the orthogonal curvilinear grid. This is different from the results obtained from both the experiment and computation on the Cartesian grid. These small disturbances are probably caused by the "rounded" tip of leading edge. Another possible reason is that the grid resolutions near the solid wall for the Cartesian case are not enough to capture these small disturbances. Waniewski et al. (2002) postulated that the surface disturbances on the wave are gravity waves which propagate along the bow wave crest. A similar situation is described by Longuet-Hinggins (1995) in the analytical discussion of the disintegration of the jet in a plunging breaker. It was assumed a perturbation in the form of surface waves (gravity-capillary wave) which propagate across the jet surface. As the wave overturns and the jet is stretched, the gravity dominant wave changes to capillary dominant wave. The jet is further stretched and liquid sheet can be pinched into "finger-shaped" jets and "cylindrical drops". Waniewski et al. (2002) also discussed another possibility that the disturbance may originate from an instability in the flow as it passes the solid surface, although no instability theory was provided.

The mechanism of the liquid sheet disturbance, fingering, pinching off drops and spray formation has not been thoroughly studied. A large amount of work has been devoted to investigating droplet spray formation of liquid jets and sheets in the fields of combustion, coating and spray painting, ink jet printing, cooling in nuclear and chemical engineering, etc., which offers useful knowledge to help to study the physics of bow wave sprays. Various regimes (scaled by *Re, We, Fr*) of breakup of liquid jets injected into gases are discussed in the study by Lin and Reitz (1998). Further experimental and computational investigations of these phenomena are needed in the future work.

Plunging Wave Breaking and Air Entrainment

Figure 5 shows the slices of the wave profile cut perpendicular to the side wall of the wedge. The liquid film, overturning jet and plunging, and air entrainment at various *x* positions are demonstrated.

As shown in the figure, at the leading edge the liquid film is very thin, which is around 3~4 mm (at x =0.05 m) for the case on the fine orthogonal grid. The thickness increases with the distance from the leading edge. It overturns when the thickness reaches 6~7cm. The thickness of the liquid film along the side wall of the wedge is shown in Figure 6 for difference cases. It can be seen that the thickness of the liquid film increases almost linearly with the distance from the

leading edge of the wedge. For the cases with different grids, the thickness is thinner on the fine grid than the coarse grid, which indicates the effect of the grid resolutions near the side wall of the wedge. The figure also shows that the wave separates earlier from the wedge on the coarse grid than on the fine grid. The thickness of the liquid sheet is not reported in experimental study (Waniewski et al., 2002). There are no experimental data available for comparison.

When the wave crest overturns, a liquid sheet is formed and breaks up into droplets before it plunges on the undisturbed water surface. After the jet hits the water surface, an oblique splash is created and a vertical jet can also be seen in the last frame of the figure. These phenomena of the wave breaking process are very similar to those observed in the plunging wave breaking studies (Peregrine, 1983; Bonmarin, 1989; Tallent et al., 1990; Wang et al., 2009). However, the bow waves are continuously plunging breaking waves and also highly three-dimensional, which are different from most of the studies of plunging wave breakings. The plunging jet shape is also close to the experimental findings. The thickness of the jet is approximately 1.5 cm to 3.5 cm and the impingement angle of the jet, β, relative to the undisturbed free surface is about 55° (Fig. 5), which agree well with the experiments where jet thickness and impingement angle is 2.0 cm to 3.0 cm and 58°, respectively.

A large amount of air is entrapped as the liquid jet plunges, and a big "air pocket" is formed as shown in Figure 7. As shown in Figure 5, the cross section of the air pocket shows an elliptical shape. This is the primary source of air entrainment due to the impact of the plunging wave on the water surface. The resulting splashes can plunge again, which causes further air entrainment. Figure 7 clearly shows the subsequent plunges. Air can also be entrained when the droplets from the splashes hit the water surface with very small air bubbles. The big size air bubbles usually cannot sustain long, but break up into small bubbles or burst into the air. The small size bubbles can sustain a longer lifetime due to the advection in the turbulent flows. In the computational study by Carrica et al. (1999), bubbles are introduced using arbitrary bubble sources at the ship bow. It has been shown that the bubbles have significant effects on the wake. The bubble entrainment mechanism, bubble sizes and distributions and their effects on the flow field need further investigations.

Wave Contact Line Elevation

The wave contact line elevations along the wedge side starting from the leading edge for different cases compared with the experimental measurements are shown in Figure 8. Both the experimental results for the towing tank model and the flume model are included in the figure. As shown in the figure, the maximum height of the flume case is below the towing tank case. Waniewski (1999) explained that this discrepancy might be due to the camera orientations which might not be exactly perpendicular to the model and parallel with the undisturbed free surface.

The overall wave contact line profiles from both the simulations and experiment have the similar trend. For the coarse Cartesian grid, the wave height is far below the experimental results. With increased grid resolutions near the wall, the wave height increases significantly. In order to further increase the grid resolutions near the solid wall, the orthogonal curvilinear grid is used. Grid refinement near the solid wall is much easier for the curvilinear grid than the Cartesian grid. The wave height computed on the orthogonal curvilinear grid is greatly increased, which is very close to the flume model case (Waniewski et al., 2002). However, further grid refinement on the curvilinear grid appears not to increase the wave height any more. This is probably due to the more breakups and disturbances of the wave crest on the fine grid than on the coarse grid since a thinner liquid film is obtained on the fine grid (Figure 6). Moreover, the grid is not systematically refined, the grid structures of the coarse and fine grids for the orthogonal curvilinear cases are different. Systematical grid refinement study will be conducted in the future work.

As compared to the towing tank case, all the simulations are under predicted. Except for the camera orientation problem explained by Waniewski (1999), several other reasons are likely accounting for the under-prediction of the wave elevation in the simulations. First, the grid resolutions are not enough to resolve the thin liquid sheet on the side wall of the wedge. Second, the boundary layer is not effectively resolved due to the lack of a turbulence model. Likely the velocity along the wedge side direction is over-predicted, whereas the velocity rising up in the vertical direction is under-predicted. The turbulence model developed for two-phase interfacial flows by Shirani et al. (2006) will be implemented and used in the future work. Moreover, the dynamic contact line problem is not well resolved: the dynamic contact angle is not considered in the simulations where the air/water interface is simply treated to be perpendicular to the solid wall; a non-slip rather than a Navier slip boundary condition is used at the contact line region. Wall adhesion effect due to the capillary force is not accurately implemented. All of these problems will be considered in the future studies.

Velocity Filed of the Plunging Jet

The velocity vector fields of the plunging jet at various x locations are plotted in Figure 9 with the vectors colored by the velocity component in the z direction. The impingement of the jet onto the free surface induces strong air flows as shown in Figures 9 a and b, which results in a pair of vortices immediately before the overturning jet. After the falling jet impacts onto the water surface, a strong vortex is produced due to the air entrainment (Figure 9d). A series small vortices are also generated as a result of splashes. The computed impact velocity is around 2.5 m/s, which agree very well with experimental value of 2.3 m/s reported in Waniewski et al. (2002).

CONCLUSIONS AND FUTURE WORK

Wave breakings around a wedge shaped bow are simulated using CFDShip-Iowa version 6 with the aim of investigating the wave breaking mechanism and small scale features of ship bow waves. The predicted overall bow wave profile (thin liquid sheet at the leading edge, overturning jet and plunging, and splashes at the wake), plunging jet shape, and surface disturbances on the wave crest are similar to the experimental observations. The computed jet impact angle, speed and thickness agree well with the experimental measurements. With increased grid resolution near the side wall of the wedge using the orthogonal curvilinear grid, the maximum elevation of the wave crest increases dramatically which matches the flume model case very well. However, the computed wave elevation is still below the towing tank case.

In the future work, the grid resolutions near the wall will be further increased. The Navier slip boundary condition and dynamic contact angle will be implemented in order to properly resolve the dynamic contact line problem. Two phase turbulence model will be used in order to accurately predict the boundary layer velocity. Systematical grid refinement study will also be included. Detailed studies of the mechanism of the liquid sheet disturbance, fingering, pinching off drops and spray formation, will be conducted.

APPENDIX: GOVERNING EQUATIONS ON ORTHOGONAL CURVILINEAR GRIDS

The derivation and notation for the curvilinear orthogonal coordinate by Pope (1978) are adopted.

Continuity Equation

$$\nabla(i)[u_i] = 0 \tag{17}$$

where u_i is the velocity in orthogonal coordinate ξ_i direction and $\nabla(i) = \frac{1}{J}\frac{\partial}{\partial \xi_i}\left(\frac{J}{h_i}\right)$. Also, J is Jacobian of coordinate transformation, and $h_i = \frac{\partial x_i}{\partial \xi_i}$, here x_i is a Cartesian coordinate. Jacobian J and h_i are related as follows:

$$J = h_i h_j h_k. \tag{18}$$

Momentum Equation

$$\frac{\partial u_i}{\partial t} + \nabla(j)\left[u_i u_j\right] - \frac{1}{\rho}\nabla(j)\left[\tau_{ij}\right] = -\frac{1}{\rho}\frac{\partial p}{\partial \xi(i)} + H_j(i)\left[u_j u_j - \frac{\tau_{ij}}{\rho}\right] - H_i(j)\left[u_i u_j - \frac{\tau_{ij}}{\rho}\right] + g_i \tag{19}$$

where ρ is the density, p is the pressure, t is the time, and g_i the gravity vector in the ξ_i direction. Also, $H_i(j) = \frac{1}{h_i h_j}\frac{\partial h_i}{\partial \xi_j}$ and $\partial\xi(i) = h_i \partial \xi_i$.

Also, viscous stress tensor τ_{ij} is defined as follows:

$$\tau_{ij} = (\mu + \nu_t \cdot \rho) S_{ij} \tag{20}$$

where μ is the dynamic viscosity and ν_t is the eddy viscosity. S_{ij} is the strain rate

$$S_{ij} = \frac{\partial u_i}{\partial \xi(j)} + \frac{\partial u_j}{\partial \xi(i)} - u_i H_i(j) - u_j H_j(i) + 2u_l H_i(l)\delta_{ij}. \tag{21}$$

Level Set Equation

Air-water interface is tracked by solving the level set equation

$$\frac{\partial \phi}{\partial t} + \frac{u_i \partial \phi}{\partial \xi(i)} = 0. \tag{22}$$

ACKNOWLEDGMENTS

This research was sponsored by the Office of Naval Research under Grant N00014-01-1-0073 and N00014-06-1-0420, under the administration of Dr. Patrick Purtell.

REFERENCES

Balay, S., Buschelman, K., Gropp, W., Kaushik, D., Knepley, M., Curfman, L., Smith, B. and Zhang, H. "PETSc User Manual", ANL-95/11-Revision 2.1.5, 2002, Argonne National Laboratory.

Bonmarin, P., "Geometric properties of deep-water breaking waves", J. Fluid Mech.,Vol. 209, 1989, pp.405-433.

Broglia, R., Di Mascio, A., Muscari, R., "Numerical simulations of breaking wave around a wedge", Proceedings of 25th symposium on naval

hydrodynamics, St. John's Newfoundland and Labrador, Canada, 2004.

Carrica, P.M., Drew, D., Bonetto, F. and Lahey, R.T., Jr., "A polydisperse model for bubbly two-phase flow around a surface ship", Int. J. Multiphase Flow, Vol. 25, 1999, pp. 257–305.

Choi, H. and Moin, P., "Effects of the computational time step on numerical solutions of turbulent flow", J. Comput. Phys., Vol. 113, 1994, pp. 1-4.

Falgout, R.D., Jones, J.E., and Yang, U.M., "The design and implementation of HYPRE, a library of parallel high performance preconditioners", in Numerical Solution of Partial Differential Equations on Parallel Computers, A.M. Bruaset and A. Tveito, eds., Springer-Verlag, Vol. 51, 2006, pp. 267-294.

Gilmanov, A., Sotiropoulos, F., and Balaras, E., "A general reconstruction algorithm for simulating flows with complex 3d immersed boundaries on Cartesian grids", J. Comput. Phys., Vol. 191, 2003, pp. 660-669.

Hu, C. and Kashiwagi, M., "Numerical and experimental studies on three-dimensional water on deck with a modified Wigley model", Proc. 9th Inter. Conf. Numer. Ship Hydrodynamics, Ann Arbor, Michigan, 2007.

Jiang, G.-S. and Peng, D., "Weighted ENO schemes for Hamilton-Jacobi equations", SIAM J. Sci. Comp., Vol. 21, 2000, pp. 2126-2143.

Jiang, G.-S. and Shu, C.-W., "Efficient implementation of weighted ENO schemes", J. Comput. Phys., Vol. 126, 1996, pp. 202-228.

Kandasamy, M., Xing, T., Stern, F., "Unsteady Free-Surface Wave-Induced Separation: Vortical Structures and Instabilities", Journal of Fluids and Structures, Vol. 25, Issue 2, 2009, pp. 343-363.

Kang, D.H., Longo, J., Marquardt, M., and Stern, F., "Solid/free-surface juncture boundary layer and wake with waves", Proc. 27th ONR Symposium on Naval Hydrodynamics, Seoul, Korea, 2008.

Karion, A., Fu, T. C., Sur, T.W., Rice, J.R., Walker, D.C. and Furey, D.A., "Experiment to examine the effect of scale on a breaking bow wave", Carderock Division, Naval Surface Warfare Center, Hydromechanics Research and Development report, 2004, NSWCCD-50-TR-2004/060.

Leonard, B. P., "A stable and accurate modelling procedure based on quadratic interpolation", Comput. Methods Appl. Mech. Engrg., Vol. 19, 1979, pp. 58-98

Lin, S. P., Reitz, R. D., Drop and spray formation from a liquid jet, Annual Review of Fluid Mechanics, Vol. 30, 1998, pp. 85-105.

Longo, J., Huang, H.P., and Stern, F., "Solid-fluid juncture boundary layer and wake", Experiments in Fluids, Vol. 25(4), 1998, pp. 283-297.

Longo, J., Shao, J., Irvine, M., and Stern, F., "Phase-averaged PIV for the nominal wake of a surface ship in regular head waves", J. Fluids Eng., Vol.129, 2007, pp.524-540.

Longuet-Higgins, M., "On the Disintegration of the Jet in a Plunging Breaker", Journal of Physical Oceanography, Vol. 25, 1995, pp. 2458–2462.

Mattor, N., Williams, T.J., and Hewett, D.W., "Algorithm for solving tridiagonal matrix problems in parallel," Parallel Comput., Vol. 21, 1995, pp. 1769-1782.

Metcalf, B., Longo, J., Ghosh, S., Stern, F., "Unsteady free-surface wave-induced boundary-layer separation for a surface-piercing NACA 0024 foil: towing tank experiments", J. Fluids Struct., Vol. 22, 2006, pp. 77-98.

Noblesse, F., Delhommeau G., Guilbaud, M., Hendrix, D., Yang, C., "Simple analytical relations for ship bow waves", Journal of Fluid Mechanics, Vol. 600, 2008, pp. 105-132.

Olivieri, A., Pistani, F., Wilson, R., Campana, E., and Stern, F., "Scars and vortices induced by ship bow wave breaking", J. Fluids Eng., Vol. 129, 2007, pp. 1445-1459.

Peng, D., Merriman, B., Osher, S., Zhao, H., and Kang, M., "A PDE-based fast local level set method", J. Comput. Phys, Vol. 155, 1999, pp. 410-438.

Peregrine, D. H., "Breaking Waves on Beaches", Ann. Rev. of Fluid Mech., Vol. 15, 1983, pp. 149-178.

Pope, S. B., "The calculation of turbulent recirculating flows in general orthogonal coordinates", J. Comput. Phys., Vol. 26, 1978, pp. 197-217.

Shu, C. W. and Osher, S., "Efficient implementation of essentially non-oscillatory shock-capturing schemes," J. Comp. Phys., Vol. 77, 1988, pp. 439-471.

Sreedhar, M. and Stern, F., "Large Eddy Simulation of Temporally Developing Juncture Flows," International Journal of Numerical Methods in Fluids, Vol. 28, No. 1, 1998a, pp. 47-72.

Sreedhar, M. and Stern, F., "Prediction of Solid/Free-Surface Juncture Boundary Layer and Wake of a Surface-Piercing Flat Plate at Low Froude Number," ASME Journal of Fluids Engineering, Vol. 120, 1998b, pp. 354-362.

Stern, F., "Effects of Waves on the Boundary Layer of a Surface-Piercing Body," Journal of Ship Research, Vol. 30, No. 4, 1986, pp. 256-274.

Stern, F., Hwang, W.S., and Jaw, S.Y., "Effects of Waves on the Boundary Layer of a Surface-Piercing Flat Plate: Experiment and Theory,"

Journal of Ship Research, Vol. 33, No. 1, 1989, pp. 63-80.

Stern, F., Choi, J.E., and Hwang, W.S., "Effects of Waves on the Wake of a Surface-Piercing Flat Plate: Experiment and Theory," Journal of Ship Research, Vol. 37, No. 2, 1993, pp. 102-118.

Stern, F., Longo, J., Zhang, Z.J., and A.K. Subramani, "Detailed bow-flow data and CFD of a Series 60 CB = .6 ship model for Froude number .316", J. Ship Res., Vol. 40, 1996, pp. 193-199.

Suh, J., Wang, Z., Yang, J., Koo, B., Stern, F., "Sharp Interface Large-Eddy Simulation of Breaking Waves by an Interface Piercing Body in Orthogonal Curvilinear Coordinates", Journal of Computational Physics (in preparation), 2010.

Sussman, M., "A parallelized, adaptive algorithm for multiphase flows in general geometries," Comp. Struct., Vol. 83, 2005, pp. 435-444.

Sussman, M., Smereka, P. and Osher, S., "A level set approach for computing solutions to incompressible two-phase flow," J. Comp. Phys., Vol. 114, 1994, pp. 146-159.

Tallent, J. R., Yamashita, T., and Tsuchiya, Y., "Transformation Characteristics of Breaking Waves", Wave Water Kinematics, Vol. 178, 1990, pp. 509-523.

Wang, Z., Yang, J., Koo, B., and Stern, F, "A coupled level set and volume-of-fluid method for sharp interface simulation of plunging breaking waves", Inter. J. Multiphase Flow, Vol. 35, 2009, pp. 227-246.

Waniewski, T., "Air entrainment by bow waves", Doctoral dissertation, 1999, California Institute of Technology, Pasadena, California.

Waniewski, T.A., Brennen, C.E. and Raichlen, F., "Bow wave dynamics", J. Ship Res., Vol. 46, 2002, pp. 1–15.

Wilson, R., Carrica, P. and Stern, F., "Simulation of ship breaking bow waves and induced vortices and scars", Int. J. Num. Meth. Fluids, Vol. 54, 2007, pp. 419-451.

Xing, T., Kandasamy, M., Stern, F., "Unsteady Free-Surface Wave-InducedSeparation: Analysis of Turbulent Structures Using Detached Eddy Simulation and Single-phase Level Set Method," Journal of Turbulence, Vol. 8, No. 44, 2007, pp. 1-35.

Yang, J., and Stern, F., "Sharp interface immersed-boundary/level-set method for wave-body inter-actions", J. Comput. Phys., Vol., 228, 2009, pp. 6590-6616.

Yang, J., Sakamoto, N., Wang, Z., Carrica, P.M. and Stern, F., "Two phase level-set/immersed-boundary Cartesian grid method for ship hydrodynamics", Proc. 9th Inter. Conf. Numer. Ship Hydrodynamics, Ann Arbor, Michigan, 2007.

Yang, J., Preidikman, S., and Balaras, E., "A strongly-coupled, embedded-boundary method for fluid-structure interactions of elastically mounted rigid bodies", J. Fluids Struct., Vol. 24, 2008, pp. 167-182.

Shirani E, Jafari A, Ashgriz N, "Turbulence models for flows with free surfaces and interfaces", AIAA Journal, Vol. 44(7), 2006, pp. 1454-1462.

Table 1 Experimental studies of bow wave breaking

		Waniewski et al. (2002)	Karion et al. (2004)
Experiment Setup	Geometry	*Deflecting plate in small & large flumes* *Wedge in a towing tank* *Half wedge angle* θ*=13˚ & 26˚* *Dihedral angle* φ*=0˚* (for *small flume,* φ*=0˚ to 15˚*)	*Bow wedge (Model No. 5605) in deep water towing basin* *Bow entrance angle* θ*=20˚ & 40˚* *Flare angle* φ*=20˚ & 0˚*
	Facility	*Small flume: 40 m long, 1.09 m wide* *Large flume:2.65 m long, 0.459 m wide* *Towing tank: 126m long, 7.5 m wide, and 3.7 m deep*	*Deep water towing basin: 575 m long, 15.5 m wide, and 6.3 to 6.5 m deep.*
	Approaches	*Contact line measured using free surface probes in the flumes* *Bow wave profile measured using videos in towing tank*	*Quantitative visualization (QViz) technique for the wave free surface* *High-speed video camera for spray of droplets*
	Test conditions	*Small flume:* $Re=1.1\times10^4$ *to* 1.6×10^4*;* $Fr=2.57$ *to 6.46* *Large flume:* $Re=1.4\times10^5$ *to* 2.0×10^5*;* $Fr=2.57$ *to 3.29* *Towing Tank:* $Re=0.43\times10^5$ *to* 7.0×10^5*;* $Fr=1.27$ *to 7.77*	$Re=4.1\times10^5$ *to* 7.0×10^6*;* $Fr=0.2$ *to 1.4* $We=11$ *to 2800*
Experimental Results & observations		*1. Bow wave profile: mainly wave elevation* *2. Plunging jet shape: jet thickness & impingement angle* *3. Scaling analysis* *4.Free surface disturbance* *5. Air entrainment (separate paper)*	*1.Contour plots of free surface elevation* *2. Surface fluctuations* *3.Surface roughness measurement* *4.Extent of breaking* *5. Spray droplets formation, number, size*
Summary		*1. The bow wave flow is highly nonlinear, there appears to be no satisfactory analytical solution.* *2. The wave is weakly dependent on dihedral angle and depends on the bow half-angle.* *3. Surface disturbances were observed, which are likely gravity waves on the surface of the bow wave. They seem to be responsible for the breakup of the jet into strings of droplets and for the periodic nature of the bubble clouds produced by the wave breaking process.*	*1. Wave breaking occurs when both Froude and Reynolds numbers exceed a critical level.* *2. A critical Webber number must be exceeded for spray generation to occur.* *3. Scaling the maximum wave heights by the quantity (* $Fr^{1.5}D$*), collapses the data fairly well.*

Table 2 Simulation cases

Cases	**Flow Conditions**	**Geometry**	**Solver**	**Grid**	**Minimum Δh (m)**
Case 1	U = 2.5 m/s, d = 0.754 m, Re = 1.64×10^5, Fr = 2.93.	Half wedge angle θ=26˚, Dihedral angle φ=0.	Cartesian	384×96×256	0.006
Case 2				512×96×192	0.003
Case 3			Orthogonal Curvilinear	384×192×192	0.0005
Case 4				512×256×256	0.00025

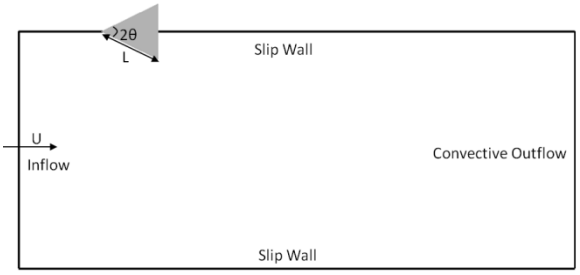

(a) Plan view of the Cartesian domain

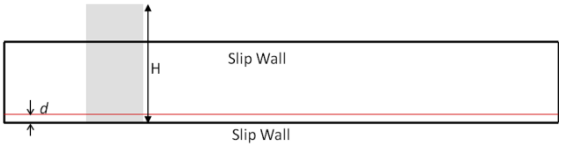

(b) Side view of the Cartesian domain

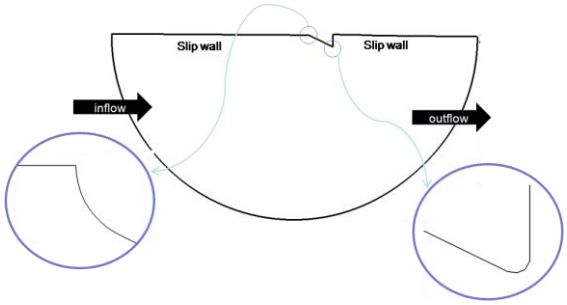

(c) Plan view of the orthogonal curvilinear domain

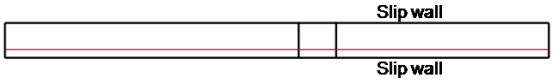

(d) Side view of the orthogonal curvilinear domain

Fig. 1. Computational domain and wedge geometry.

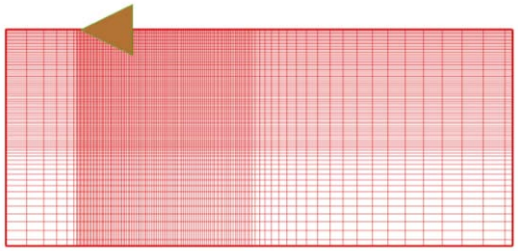

(a) Cartesian grid

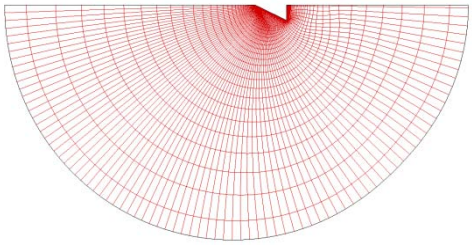

(b) Orthogonal curvilinear grid

Fig. 2. Grid structures of the wedge flow.

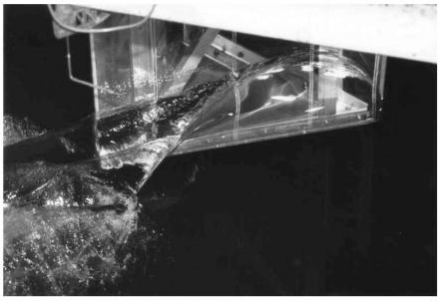

(a) Experiment (Waniewski *et. al*, 2002)

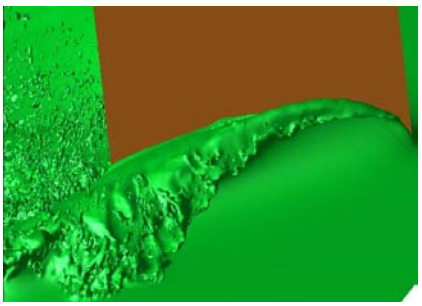

(b) Simulation (case 2)

Fig. 3. Bow wave profiles.

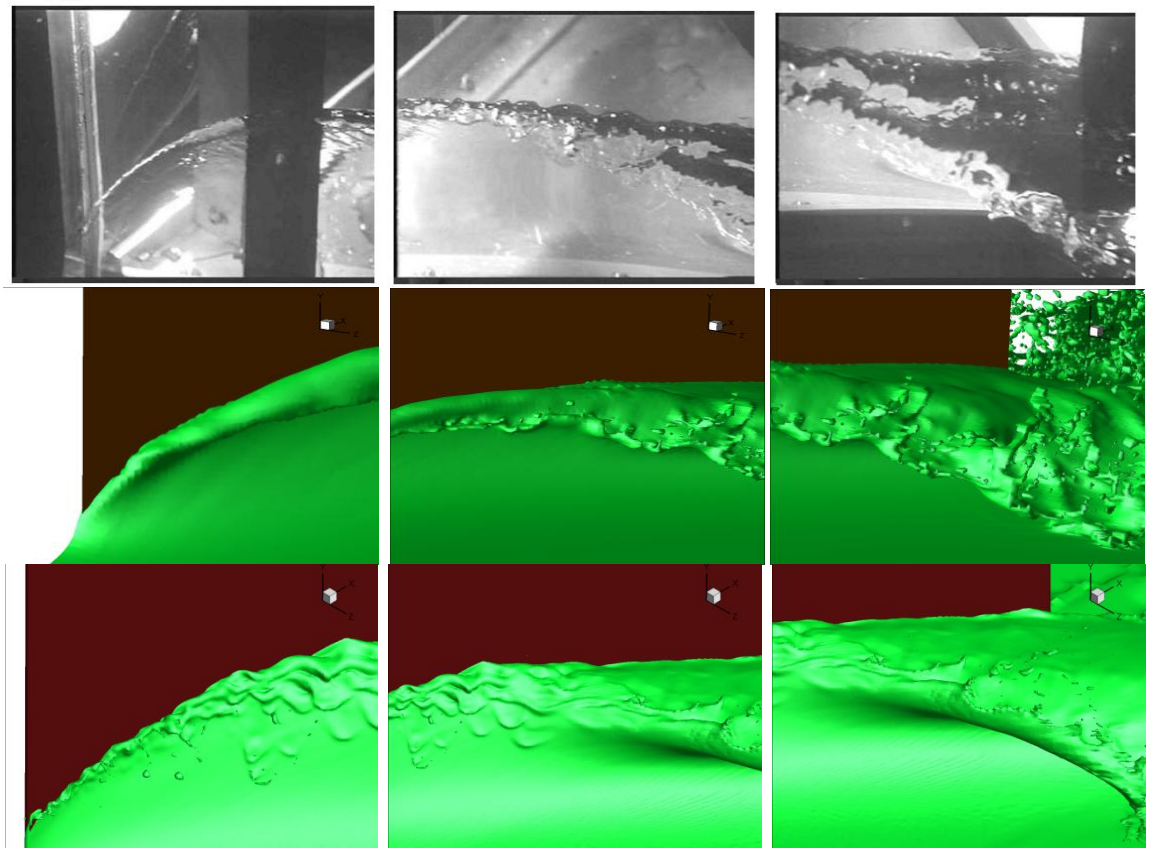

(a) Leading portion (b) Middle portion (c) Trailing portion

Fig. 4. Free surface disturbance on the wave crest. Top: Experiment (Waniewski et. al, 2002); Midddle: Simulation on Cartesian grid (case 2); Bottom: Simulation on orthogonal curvilinear grid (case 4).

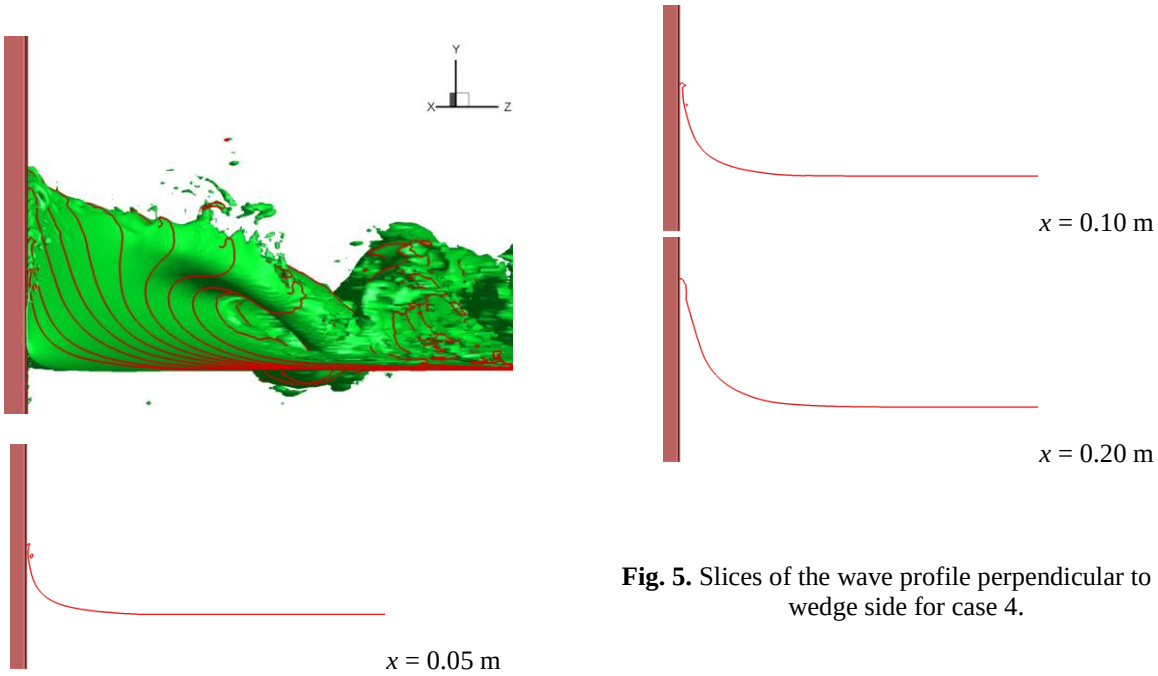

Fig. 5. Slices of the wave profile perpendicular to the wedge side for case 4.

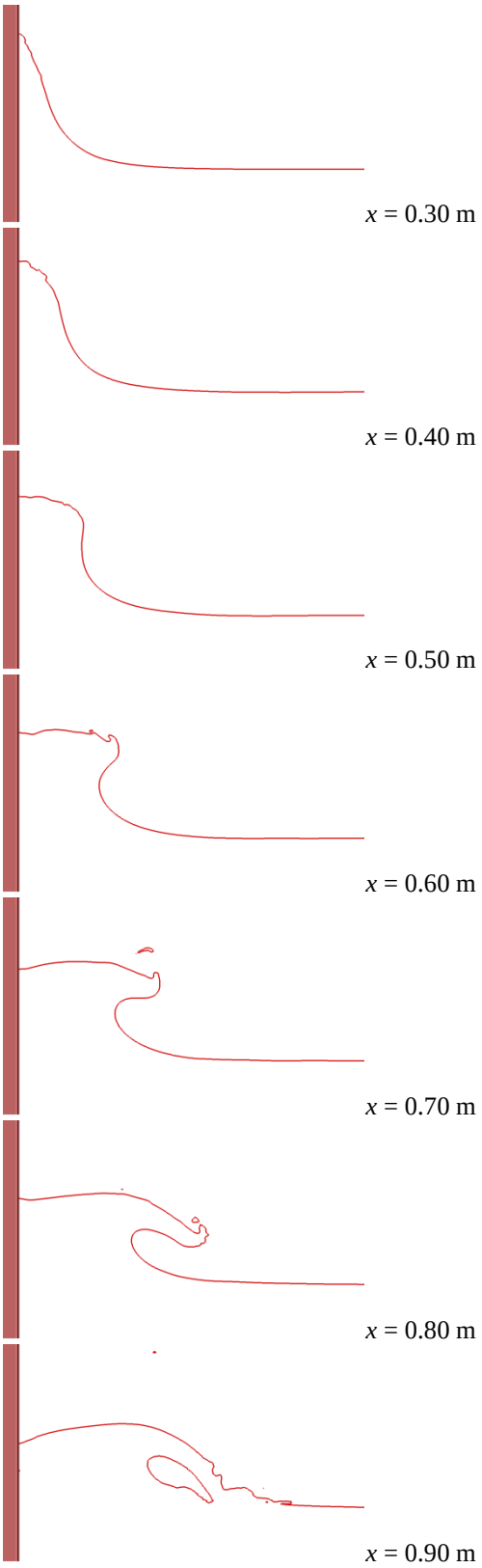

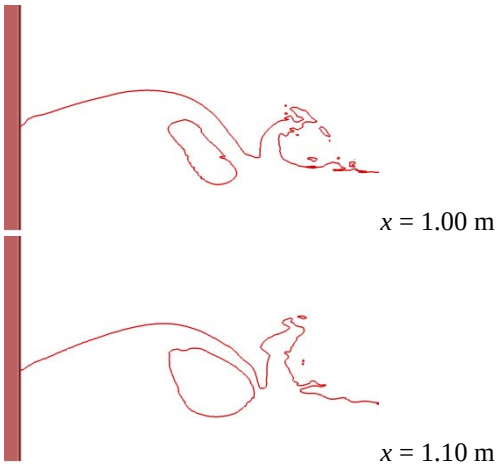

Fig. 5. (Continued)

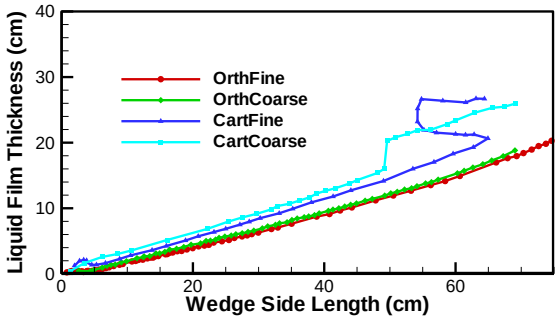

Fig. 6. Liquid film thickness along the wedge side at y = 7.97 cm.

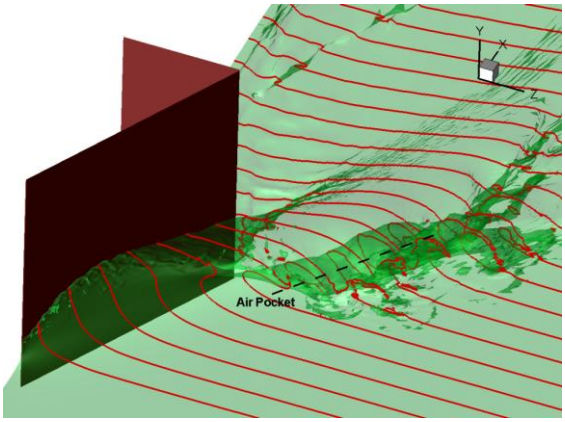

Fig. 7. Perspective view of the wave profile with slices perpendicular to x direction (case 4).

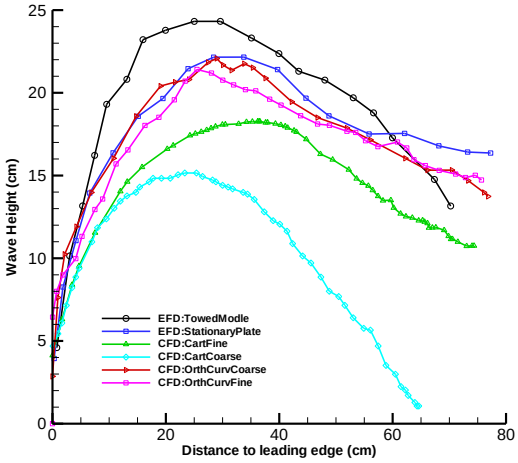

Fig. 8. Comparison of the wave profile with the experimental results (Waniewski *et. al*, 2002).

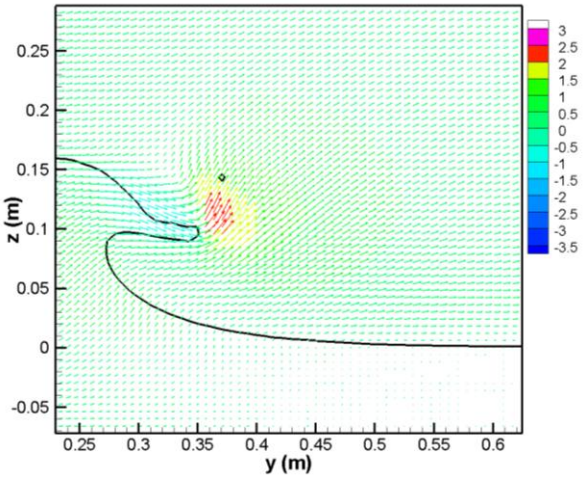

x = 0.30 m

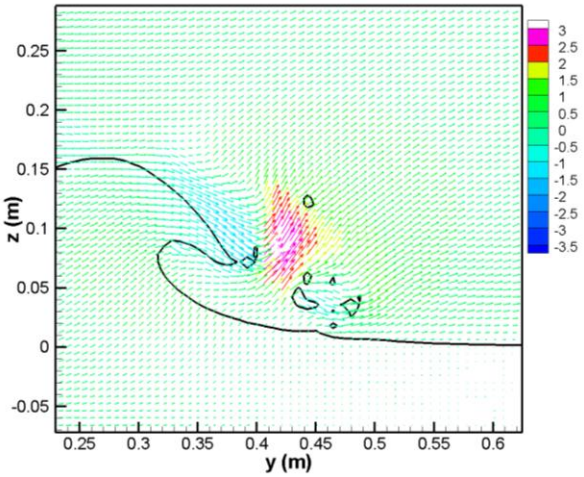

x = 0.35 m

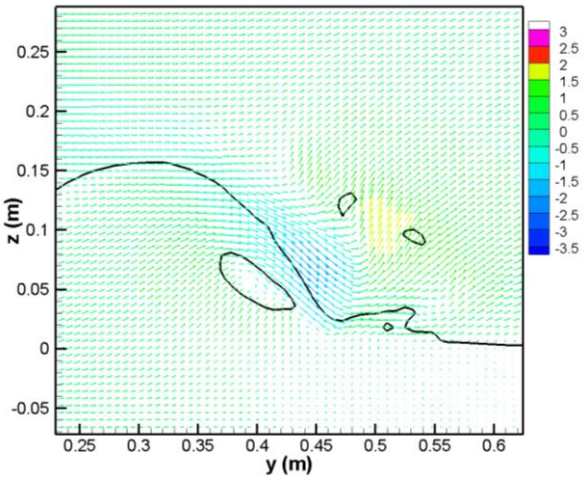

x = 0.40 m

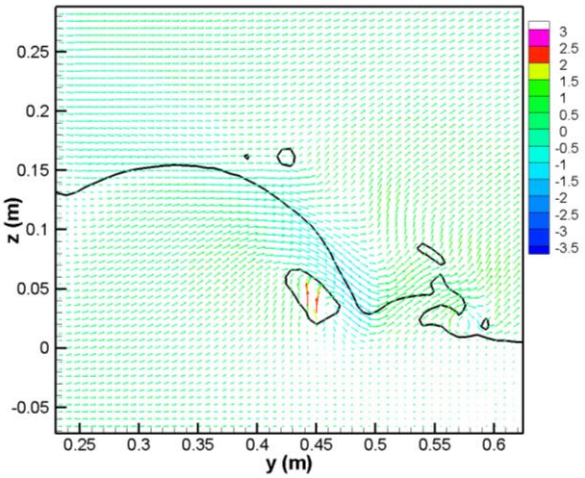

x = 0.45 m

Fig. 9. Velocity vector fields of plunging jet.